Lattice-Boltzmann Model with Sub-Grid-Scale Boundary Conditions

R. Verberg and A. J. C. Ladd*

Chemical Engineering Department, University of Florida, Gainesville, Florida 32611-6005

(Received 4 November 1999)

A lattice-Boltzmann method has been developed to incorporate solid-fluid boundary conditions on length scales less than the grid spacing. By introducing a continuous parameter, specified at each node and representing the fluid volume fraction associated with that node, we obtain second-order accuracy for boundaries at arbitrary positions and orientations with respect to the grid. The method does not require surface normals, and can therefore be applied to irregular geometries such as porous media. The new rules conserve mass and momentum, and reduce to the link bounce-back rule at aligned interfaces.

PACS numbers: 47.11.+j, 47.15.Gf, 47.55.Mh, 83.85.Pt

In this Letter we present a fundamental improvement to the conventional lattice-Boltzmann method, which incorporates information about the solid surface on scales less than the resolution of the grid. In most lattice-Boltzmann simulations the solid-fluid boundary conditions are modeled by the bounce-back rule, in which particles encountering a solid surface are reflected back in the direction they came from. However, discretization of the solid surface introduces particular problems in simulations where the surface morphology is evolving due to erosion or deposition of dissolved solids [1]. In such cases, changes to the solid surfaces cannot be modeled smoothly, but only in discrete units of the grid spacing. To simulate these systems we have devised a new boundary condition for the lattice-Boltzmann method in which the location of the solid surface can change continuously, on scales less than the grid spacing. The new boundary rules, which we call continuous bounce-back (CBB) rules, are an extension of the link or midway bounce-back (LBB) method [2] to include the reflections of distributed population densities from partially filled cells. We present numerical results that demonstrate that second-order accurate results can be obtained for flow in narrow channels where the walls are not commensurate with the grid. We also show that grid artifacts in simulations of flows past curved surfaces (disks or spheres) are much reduced by the CBB rules. Finally, we show that the flow patterns in a narrow fracture are less sensitive to grid size than in the LBB method.

In the lattice-Boltzmann method, the state of the system is characterized by the discretized velocity distribution function $n_i(\mathbf{r}, t)$, which describes the number of fluid particles at a lattice node $\mathbf{r}$ at time t with a velocity $\mathbf{c}_i$. The mass density $\rho(\mathbf{r}, t)$ and the momentum density $\mathbf{j}(\mathbf{r}, t)$ are moments of $n_i(\mathbf{r}, t)$: $\rho(\mathbf{r}, t) = \sum_i n_i(\mathbf{r}, t)$ and $\mathbf{j}(\mathbf{r}, t) = \sum_i \mathbf{c}_i n_i(\mathbf{r}, t)$. We use a volumetric interpretation [3,4] in which $n_i(\mathbf{r}, t)$ represents the mean population density in the Wigner-Seitz cell surrounding node $\mathbf{r}$. The time evolution of the distribution function in the bulk fluid is the same as in the conventional model; $n_i(\mathbf{r} + \mathbf{c}_i, t + 1) = n_i(\mathbf{r}, t) + \Delta_i(\mathbf{r}, t) + f_i(\mathbf{r}, t)$, where $f_i(\mathbf{r}, t)$ incorporates the effect of external forces. Our simulations use the Bhatnagar-Gross-Krook collision operator $\Delta_i(\mathbf{r}, t) = -\tau^{-1}[n_i(\mathbf{r}, t) - n_i^{\mathrm{eq}}(\mathbf{r})]$ and an equilibrium distribution, $n_i^{\mathrm{eq}}(\mathbf{r})$, appropriate to Stokes flow [2]. In this work we take $\tau = 1$, giving a kinematic shear viscosity $\nu = 1/6$.

To simulate the interactions between fluid and solid, the lattice-Boltzmann model must be modified to incorporate the boundary conditions imposed on the fluid by the solid phase. Our new scheme is based on the link bounce-back method, in which the boundary nodes lie midway between the solid and fluid nodes [2]. For planar surfaces it can be shown that the hydrodynamic boundary is located at the boundary nodes, with deviations that are second order in the lattice spacing [5]. Several other methods to obtain second-order accurate boundary conditions have been suggested in the literature [6–12], but they are not easily applied to irregular geometries. The method described in this Letter is fundamentally different from most previous schemes in that it attempts to model solid-fluid surfaces that are not mapped directly onto the lattice grid. In addition, it shares the important advantage of the bounce-back rule that it does not require surface normals. Instead, we introduce a continuous variable, $\alpha(\mathbf{r})$, specified at each node and representing the fluid volume fraction associated with that node, and then construct rules relating the velocity distribution function after propagation, $n_i(\mathbf{r} + \mathbf{c}_i, t + 1)$, to the postcollision distribution $n_i^*(\mathbf{r}, t) = n_i(\mathbf{r}, t) + \Delta_i(\mathbf{r}, t) + f_i(\mathbf{r}, t)$.

We begin with an extension of the LBB method to two-dimensional channel flows where the solid-fluid boundaries are parallel to a lattice symmetry direction, but are not necessarily commensurate with the cell boundaries. We introduce the basic concepts by assuming that the population densities are uniformly distributed throughout the volume of the cell surrounding each node. Particles are propagated from each point in a cell by one lattice spacing per time step. If the channel wall coincides with a face of a cell, we have the typical LBB rule [cf. Fig. 1(a)]. Here, $n_1^*(\mathbf{r}_1, t)$ is completely reflected at the interface between cells 1 and 2, so that $n_2(\mathbf{r}_1, t + 1) = n_1^*(\mathbf{r}_1, t)$. If cell 2 instead contains a fraction of fluid α_2 [cf. Fig. 1(b)], $n_1^*(\mathbf{r}_1, t)$ is split into three different fractions, each one

 0031-9007/00/84(10)/2148(4)$15.00

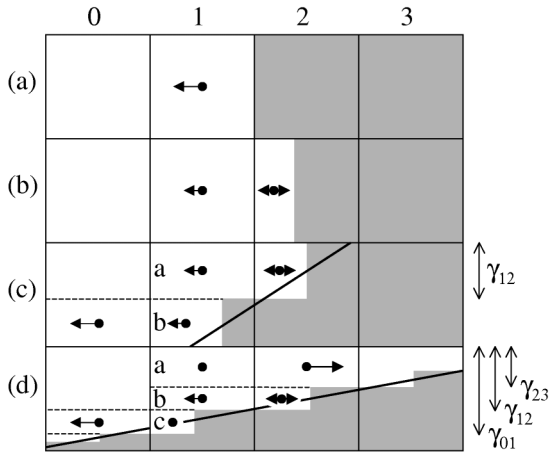

FIG. 1. Schematic representation of the different geometries discussed in the text. The gray areas represent the solid phase, the arrows indicate the population densities after propagation of $n_1^*(\mathbf{r}_1, t)$, and the solid dots indicate the location of the mean population density in each cell or fraction of a cell. The population densities n_1 and n_2 are moving to the right and left, respectively. The heavy lines in (c) and (d) indicate an inclined boundary represented by the sequence of partially filled cells.

translating over a distance of one lattice spacing and reflecting at the solid-fluid interface at the appropriate time, i.e., for $\alpha_2 < 0.5$ [cf. Fig. 1(b)],

$$n_1(\mathbf{r}_2, t + 1) = n_1^*(\mathbf{r}_1, t), \tag{1a}$$

$$n_2(\mathbf{r}_2, t + 1) = n_1^*(\mathbf{r}_1, t), \tag{1b}$$

$$n_2(\mathbf{r}_1, t + 1) = (1 - 2\alpha_2) n_1^*(\mathbf{r}_1, t) + \alpha_2 [n_1^*(\mathbf{r}_2, t) + n_2^*(\mathbf{r}_2, t)]. \tag{1c}$$

If cell 2 is more than half full of fluid ($\alpha_2 > 0.5$) none of the reflected population density is returned to cell 1, and Eqs. (1b) and (1c) must be modified accordingly. Equation (1) correctly accounts for the mass transfer between cells of different fluid fractions and reduces to the LBB rule [Fig. 1(a)] when $\alpha_2 \to 0$. However, the fluid velocity in the partially filled cells is only first-order accurate.

We proceed to a better approximation by taking into account the velocity gradient in the direction of propagation. Assuming that the population density varies linearly along the line connecting cells 1 and 2,

$$n_i^*(x, t) = \frac{2x}{1 + \alpha_2} [n_i^*(\mathbf{r}_2, t) - n_i^*(\mathbf{r}_1, t)] + n_i^*(\mathbf{r}_1, t), \tag{2}$$

for $i = 1, 2$. Here we have taken the origin at the center of cell 1, with the positive x axis pointing in the $\mathbf{c}_i$ direction. The mean population density of cell 2 lies midway between the wall and the interface between cells 1 and 2, as shown in Fig. 1(b). The propagation of $n_i^*(x, t)$ from each location, x, again consists of a translation in the direction of $\mathbf{c}_i$ over a distance of one lattice spacing and reflection at the interface at the appropriate time. An example of the resulting propagation rule is

$$n_1(\mathbf{r}_2, t + 1) = \frac{1}{\alpha_2} \int_{-1/2}^{\alpha_2 - 1/2} n_1^*(x, t)\, dx = \frac{2n_1^*(\mathbf{r}_1, t) + (\alpha_2 - 1) n_1^*(\mathbf{r}_2, t)}{\alpha_2 + 1}; \tag{3}$$

the other integrals can be evaluated in a similar fashion.

The CBB rules were tested for Poiseuille flow in channels that were shifted with respect to the underlying lattice. In Fig. 2(a), we show the flow profile for Poiseuille flow in a channel of width $L = \sum_{\mathbf{r} \in L} \alpha(\mathbf{r}) = 3$, driven by a pressure gradient $\nabla_y p$. It can be seen that even for a narrow channel the agreement with the analytic result is good; the largest deviations occur for channels shifted by one-half of a lattice spacing and are of the order of 10%. The mean relative error in the flow profile, $\epsilon(L) = \{L^{-1} \sum_{\mathbf{r} \in L} \alpha(\mathbf{r}) [j_y(\mathbf{r}, L) - j_y(\mathbf{r}, L \to \infty)]^2\}^{1/2} / j_0$, decreases as $1/L^2$, as shown in Fig. 2(b). For $L \geq 5$, $\epsilon(L)$ is less than 4%, while the error in the location of the hydrodynamic boundary is less than 0.05 lattice spacings. We obtained similar results for Poiseuille flow in channels of noninteger widths.

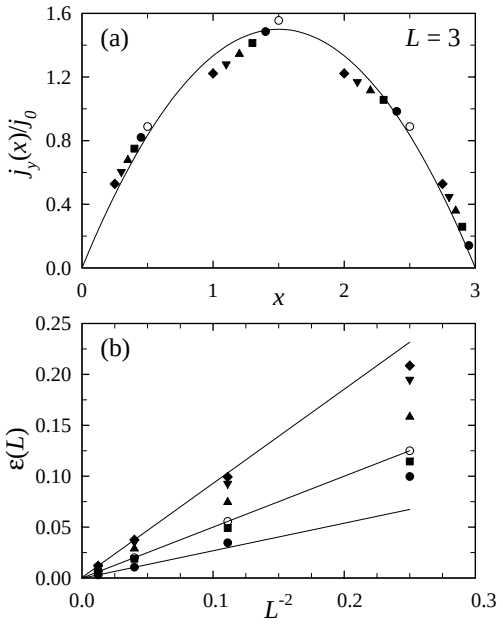

FIG. 2. Poiseuille flow in a shifted channel. (a) Flow profile $j_y(x)$ for a channel width $L = 3$; the theoretical mean momentum flow $j_0 = L^2 \nabla_y p / 12\nu$. (b) Mean relative error $\epsilon(L)$ in the flow profile. The open circles are the simulation results for a lattice where the wall coincides with the interface between two cells. The solid symbols are for lattices shifted with respect to the wall in increments of 1/10: in increasing order these go from solid circles (0.1) to diamonds (0.5). The solid lines indicate the asymptotic $1/L^2$ decay of $\epsilon(L)$.

In most situations of practical interest the system changes rapidly from fluid to solid, typically with only one partially filled cell in between. However, more complicated geometries do arise, in which the solid-fluid interface extends over more than one cell. We approximate an inclined boundary extending over two cells by the geometry shown in Fig. 1(c), so that during the propagation step a fraction of the population density is reflected in cell 1, while the remainder bounces back in cell 2. The propagation rule for $n_1^*(\mathbf{r}_1, t)$ now consists of the sum of two contributions, each of them determined by the same basic rules discussed in reference to Fig. 1(b). The fluid fraction (a) is updated by substituting α_2/γ_{12} for α_2 in Eq. (3) and the analogous expressions for $n_2(\mathbf{r}_2, t + 1)$ and $n_2(\mathbf{r}_1, t + 1)$; $\gamma_{12} = (\alpha_1 + \alpha_2)/2$ sets the barrier height across the boundary between cells 1 and 2. In the geometry shown in Fig. 1(c), if the wall defining (b) is separated by less than half a lattice spacing from the interface between cells 0 and 1, the fluid fraction (b) is totally reflected, and then propagated to cell 0.

We have performed a series of tests for Poiseuille flow in inclined channels, where the boundaries and pressure gradient were placed at an angle θ with respect to one of the lattice vectors; in one case $\tan(\theta) = 3/4$ and $L = 24/5$ and $48/5$, and in the other case $\tan(\theta) = 1$ and $L = 7/\sqrt{2}$ and $14/\sqrt{(2)}$. For both inclinations, $\epsilon(L)$ was about 8% for the smaller channel width and 3% for the larger. In contrast, the LBB method is very sensitive to the location of the interface relative to the position of the nodes. For example, for $\tan(\theta) = 1$ and $L = 7/\sqrt{2}$, the flow profile is about 40% too large if the half-occupied boundary cells are considered to be fluid and about 50% too small if they are treated as solid.

A drawback of the proposed boundary condition is that the limits for $\alpha_1 \to 1$ or $\alpha_2 \to 0$ are not continuous; the shoulder in cell 2 of height $1 - \gamma_{12}$ [Fig. 1(c) vanishes discontinuously when $\alpha_1 = 1$. Although a different choice of γ_{12} can prevent this discontinuity, we made this particular choice to maintain a continuous profile in the general case shown in Fig. 1(d). We have numerically tested the impact of this discontinuity and found that it is small.

Finally, we consider the most general geometry, shown schematically in Fig. 1(d). Here we consider only the case $\alpha_1 > \alpha_2$; the update rule for $\alpha_1 \le \alpha_2$ is full propagation with mass conservation, i.e., $n_1(\mathbf{r}_2, t + 1) = \alpha_1 n_1^*(\mathbf{r}_1, t)/\alpha_2$. Although Fig. 1(d) is drawn for $\alpha_0 > \alpha_1$ and $\alpha_2 > \alpha_3$, our results are equally valid for arbitrary values of α_0 and α_3. The propagation rule for the postcollision distribution in cell 1 now consists of the sum of three contributions. The fluid fraction (a) is propagated to cell 2, while the fractions (b) and (c) are updated in a manner similar to that described for the two cell case [Fig. 1(c)]. The complete CBB rules, including limiting cases, will be discussed in detail in a future publication.

We tested the most general CBB rules by simulating fluid flow through periodic arrays of disks and spheres, which utilize a mixture of the different types of boundary configurations. In each case we have calculated the mean momentum flow $\langle j_y \rangle = V^{-1} \sum_{\mathbf{r} \in V} \alpha(\mathbf{r}) j_y(\mathbf{r})$ in a unit cell of length L, driven by a pressure gradient $\nabla_y p$. In Fig. 3, we plot the reduced drag coefficient $F_D = -L^2 \nabla_y p / \nu \langle j_y \rangle$ of a square array of disks as a function of the radius of the disk $R = 3L/8$. The results show two important improvements over the LBB method: (i) The drag coefficient obtained with the CBB rules is virtually independent of the position of the center of the disk with respect to the lattice, and (ii) the error in F_D is much smaller and the convergence to the asymptotic value is second order. For a cubic array of spheres the spread in F_D was even smaller than for disks, most probably due to a higher degree of averaging over the different types of boundaries.

The CBB rules have also been tested by simulating fluid flow in a realistic fracture geometry. A marble cylinder was split into two halves and the surface profile of each half was measured using mechanical profilometry [14]. By replacing the two halves with a small offset, an irregular fracture profile was obtained with a mean fracture height $H = 0.324$ mm. The dimensions of the sample were $32 \times 32 \times 4$ mm. The in-plane resolution of the profilometer was 0.25 mm and the height measurement was accurate to about 15 μm. The flow was driven by a pressure gradient $\nabla_y p$, and the sample was jacketed around the xy and yz faces. An 0.25 mm thick fluid layer was added to each end of the specimen in the flow (y) direction and periodic boundary conditions were applied. The

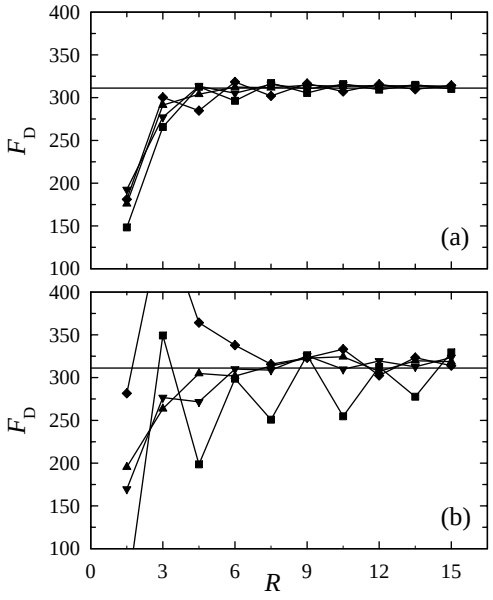

FIG. 3. Reduced drag coefficient F_D of a square array of disks, obtained with the CBB rules (a) and LBB rules (b), for different positions of the center of the disk with respect to the lattice: in the center of a cell (◆), in the corner of a cell (■), and at two random positions (▲ and ▼). The solid line is the theoretical result [13] at the same porosity, $9\pi/64 = 0.442$.

steady state momentum density $\mathbf{j}(\mathbf{r})$ was integrated over a column spanning the entire height of the fracture to give the total in-plane momentum flow $\mathbf{j_p}(\mathbf{r})$. Three different spatial resolutions Δ_0/n were used, with $\Delta_0 = 0.25$ mm and $n = 1, 2,$ and 4. To compare results at different spatial resolutions a constant cross section of 0.25×0.25 mm was used for each column; results at the higher resolutions $n = 2$ and 4 were therefore averaged over blocks of 4 and 16 columns, respectively. Since the mean fracture height is small, an accurate simulation of the flow in this geometry would seem to require a much higher resolution in the height (z direction) than in the horizontal (xy) plane. However, results obtained using the CBB rules show that accurate flow profiles can be obtained with only 2–3 cells across a typical channel width; the LBB method requires about twice as many cells for comparable accuracy.

In Fig. 4(a), we plot the y component of the mean flow $\langle j_{\mathbf{p},y} \rangle$ and the flow field $j_{\mathbf{p},y}(\mathbf{r})$ at two random positions. The discretization inherent in the LBB method causes the narrowest channel to be completely blocked at the lowest resolution, whereas the CBB rules already give a reasonable momentum flow. Figure 4(b) shows that the CBB rules describe the rms velocity fluctuations with a mean error of about 10% at the lowest resolution, whereas with the LBB method the error is almost 80%. Contour plots of the flow field illustrate this point more clearly [15]. Using the CBB rules, the lowest resolution simulation contains most of the details of the flow field, although the average height of the fracture is only about 1.3 lattice spacings.

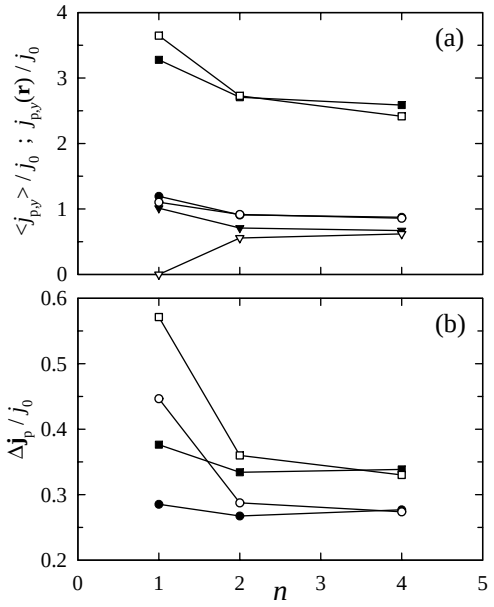

FIG. 4. (a) The mean flow $\langle j_{\mathbf{p},y} \rangle / j_0$ (circles) and flow field $j_{\mathbf{p},y}(\mathbf{r})/j_0$ at two random positions, one where the fracture height is approximately half (triangles) and one where it is approximately double (squares) the mean fracture height. (b) Velocity fluctuations perpendicular ($\Delta j_{\mathbf{p},x}/j_0$: circles) and parallel ($\Delta j_{\mathbf{p},y}/j_0$: squares) to $\nabla_y p$. Here, $j_0 = H^2 \nabla_y p / 12\nu$, with the mean fracture height $H = 0.324$ mm. The open and closed symbols are simulation results using the LBB and the CBB rules, respectively.

In this Letter we have introduced a new set of boundary rules for the lattice-Boltzmann model, which allow for a reduction in resolution by a factor of 2 to 4; in three dimensional simulations a factor of 2 reduction in resolution translates into at least a 16-fold reduction in computer time and an 8-fold reduction in memory. Although the continuous bounce-back rules are more complicated to implement, the additional computational overhead is small. The key advance is that the accuracy of the new boundary conditions is insensitive to the actual position of the interface with respect to the lattice. We anticipate that the most important applications of this idea will be to simulations of changes in morphology in porous media, arising from erosion or deposition of solid carried by the fluid. The method can be adopted to simulations of particle suspensions by modifying the reflected population densities to take account of the moving interface [2].

We thank Dr. William Durham (Lawrence Livermore National Laboratories) for providing us with the fracture-image data. This work was supported by the U.S. Department of Energy, Office of Basic Energy Sciences (DE-FG02-98ER14853).

*Electronic address: tladd@ufl.edu

[1] J. A. Kaandorp, C. P. Lowe, D. Frenkel, and P. M. A. Sloot, Phys. Rev. Lett. **77**, 2328 (1996).
[2] A. J. C. Ladd, J. Fluid Mech. **271**, 285 (1994).
[3] R. Benzi, S. Succi, and M. Vergassola, Phys. Rep. **222**, 145 (1992).
[4] H. Chen, Phys. Rev. E **58**, 3955 (1998).
[5] X. He, Q. Zou, L.-S. Luo, and M. Dembo, J. Stat. Phys. **87**, 115 (1997).
[6] P. A. Skordos, Phys. Rev. E **48**, 4823 (1993).
[7] D. R. Noble, S. Y. Chen, J. G. Georgiadis, and R. O. Buckius, Phys. Fluids **7**, 203 (1995).
[8] T. Inamuro, M. Yoshino, and F. Ogino, Phys. Fluids **7**, 2928 (1995).
[9] R. S. Maier, R. S. Bernard, and D. W. Grunau, Phys. Fluids **8**, 1788 (1996).
[10] S. Chen, D. Martinez, and R. Mei, Phys. Fluids **8**, 2527 (1996).
[11] Q. Zou and X. He, Phys. Fluids **9**, 1591 (1997).
[12] H. Chen, C. Teixeira, and K. Molvig, Int. J. Mod. Phys. C **9**, 1281 (1998).
[13] A. S. Sangani and A. Acrivos, Int. J. Multiph. Flow **8**, 193 (1982).
[14] W. B. Durham and B. P. Bonner, Int. J. Rock Mech. Min. Sci. Geomech. Abstr. **30**, 699 (1993).
[15] These contour plots may be seen at www.che.ufl.edu/ladd/Research/Porous/SubGrid.htm.